A sub-stepping iterative constitutive model for cyclic cracking-crushing-shearing in masonry interface elements

Xie, Z.; Sousamli, M.; Messali, F.; Rots, J. G.

DOI
10.1016/j.compstruc.2021.106654

Publication date
2021

Document Version
Final published version

Published in
Computers and Structures

Computers and Structures 257 (2021) 106654

Contents lists available at ScienceDirect

Computers and Structures

journal homepage: www.elsevier.com/locate/compstruc

A sub-stepping iterative constitutive model for cyclic cracking-crushing-shearing in masonry interface elements

Z. Xie, M. Sousamli *, F. Messali, J.G. Rots

Faculty of Civil Engineering & Geosciences, TU Delft, Delft, the Netherlands

ARTICLE INFO

Article history:
Received 8 January 2021
Accepted 5 August 2021

Keywords:
Constitutive-model
Masonry
Micro-modelling
Interface elements
Sub-stepping

ABSTRACT

This paper proposes a sub-step based iterative constitutive model for line interface elements used to analyse masonry structures loaded in-plane. Based on a total deformation theory, the model adopts characteristics of multi-surface plasticity, including a Coulomb friction failure surface for shear, with tension and compression cut-off and softening for all three domains. The model is driven by two damage parameters, one for compression and one that couples tension and shear. The sub-stepping technique is demonstrated to be numerically stable and is used as an alternative to the traditional return-mapping algorithms, which are prone to convergence issues and instability. The proposed model has been validated against experimental tests performed on masonry walls subjected to cyclic, in-plane loading. The numerical simulations adequately identify the failure mode, the hysteretic behaviour and the crack pattern. When toe crushing is governing, the results appear to be sensitive to the assumed masonry compressive strength. It is shown that calibration of the lumped compressive strength makes possible to fully describe the damage evolution in walls that exhibit a mix of flexural crack-crush failure and shear failure. Overall, the model is demonstrated to be an efficient and robust tool for analysing the cyclic, in-plane behaviour of masonry walls.

1. Introduction

Masonry is one of the oldest building materials in the world, encountered in a variety of structures, from historic monuments to modern residential buildings. It is typically made of units (bricks, stones, blocks or other) and joints (mortar or dry), being an inhomogeneous material with complex mechanical behaviour. Despite its good performance under gravitational loads, it is susceptible to damage when subjected to other types of loads, from settlements to more exceptional loads, such as earthquakes. In those cases, its failure is usually brittle, and the cracks can develop along the joints or through the units, depending on the strength of the two components and their interfaces.

Different modelling strategies are traditionally applied for the numerical analysis of masonry structures, depending on the desired level of accuracy and computational effort, and on the knowledge of the structure's geometry and of the material properties. Classifications and reviews of these strategies according to different authors can be found in [3–5]. According to the classification of Lourenco and Rots for Finite Element Modelling (FEM) of masonry [6–8], three approaches are commonly used: macro-modelling, detailed micro-modelling and simplified micro-modelling. In macro-modelling, masonry is assumed to be a homogeneous material and its properties and damage are smeared out in the continuum; it has been observed that the continuum constitutive models best describe the behaviour of masonry when the orthotropy of masonry is taken into account [9–17]. In detailed micro-modelling, the units and the mortar are modelled with continuum elements, whereas the unit-mortar interfaces are represented by discontinuum interface elements. Finally, simplified micro-modelling lumps the properties of the mortar joints and the unit-mortar interfaces at either side of the joint into zero-thickness interface elements. The units are then properly increased in thickness by adding the joint thickness to them, so that the stack of units and zero-thickness interfaces has the same dimensions as the real masonry. Simultaneously, the elastic stiffness of the zero-thickness interface is determined from the Young's modulus of the joint and the Young's modulus of the unit, such that it matches the actual overall Young's modulus of the masonry as a composite [8]. Macro-models are more suitable for applications on structures of large dimensions, since they offer a good compromise between accuracy and numerical effort. Conversely, the micro-models are usually more accurate, even though they require more computational time and memory.

* Corresponding author.

https://doi.org/10.1016/j.compstruc.2021.106654
0045-7949/

The need for higher accuracy and the necessity to examine in more detail the local behaviour of masonry has led to the development of constitutive models for interface elements, broadly used for applications on masonry structures. One of the first constitutive models for masonry interface elements was developed by Lotfi et al. [18]. Another early application was the multi-surface plasticity model of Lourenco and Rots [1], developed initially for monotonic cases and extended later on to include also cyclicity [19]. Since then, more constitutive models have been developed [20–29], all of them incorporating a Coulomb friction failure criterion. Even though these models have the potential to provide accurate results, the convergence difficulties and numerical instabilities that arise during the return-mapping algorithm are a recurring problem of plasticity-based models, especially in high curvature yield functions or in the case of multi-surface plasticity with "corners" [30–33]. Moreover, the accuracy of implicit return mapping schemes is not always reliable if the strain increments are not sufficiently small. An alternative method proposed for these problems is the sub-stepping technique, where the strain increments (or, more precisely, relative displacement increments in case of interfaces) are divided into smaller sub-steps and integration is conducted at each sub-step [34–37].

The aim of the authors is to provide a constitutive model for 1D line interface elements capable of modelling the failure modes of masonry while maintaining numerical stability. To this extent, this paper proposes a sub-stepping based iterative constitutive model based on total deformation theory, while adopting some characteristics of multi-surface plasticity, naming yield-surface criteria including Coulomb friction, as well as tension and compression cut-off including softening. To clarify, interface models based on deformation theory express the tractions as a function of the total relative-displacements (in analogy to the total strain crack models used in continuum elements), whereas in classical multi-surface plasticity theory the total displacements (or strains for continuum elements [38]) are decomposed in an elastic and a plastic part [39]. Additionally, in order to include the strength and stiffness degradation, two damage parameters are introduced: one coupled parameter for tension and shear, and one for compression. The combination of the aforementioned characteristics resembles the damage-plasticity algorithms and this name will be adopted from hereon to describe the constitutive model, keeping in mind that the formulation of the stresses is based on a total relative-displacement concept. The novelty of the model lies on the inclusion of two algorithms: a sequential uniaxial damage calculation algorithm in normal and shear directions, followed by an extra damage iterative calculation algorithm. These algorithms in combination with the sub-stepping technique constitute a robust procedure and can replace the mapping-back process. Moreover, the use of a sub-stepping technique tackles issues related to path-dependency. At the current stage, the constitutive relations have been derived only for the in-plane behavior of two dimensional masonry walls.

A description of the uniaxial constitutive relations and of the multi-surface plasticity criteria is given in Sections 2 and 3 respectively, followed by the description of the sub-stepping damage-plasticity algorithm in Section 4. The validation of the proposed constitutive model against experimental results is discussed in Section 5 and the final remarks are reported in Section 6.

2. Uniaxial constitutive relations

For the description of the loading, unloading and reloading relations in compression, tension and shear, the stress–strain relationships are derived from those proposed in [16] and implemented in the Engineering Masonry Model (EMM) [40]. These equations, originally defined for continuum elements, are modified to be suitable for interface elements.

In the following, σ indicates the stress normal to the interface, τ the shear stress tangential to the interface, d_n and d_s are the relative displacements normal and tangential to the interface, respectively, whereas K indicates the stiffness of the interface. Finally, the subscripts c, t, s refer to compression, tension and shear, e, so and sec refer to elastic, softening and secant, and $peak$ and u refer to the state at the peak and at the end (ultimate) of the softening diagram respectively.

2.1. Compression

The compressive stress envelope consists of a sequence of a third-order curve, a parabolic curve up to the compressive strength f_c, and a linear softening curve, as expressed in Eq. (1).

$$\sigma = \begin{cases} B_1\left[\frac{K_{c,e}d_n}{f_c}\right]^3 - B_2\left[\frac{K_{c,e}d_n}{f_c}\right]^2 + K_{c,e}d_n & \text{for } -\frac{f_c}{K_{c,e}} \le d_n < 0 \\ \left(\frac{A-1}{A}\left(\frac{K_{c,e}\left(d_{c,peak}+d_n\right)}{K_{c,e}d_{c,peak}-f_c}\right)^2 - 1\right)f_c & \text{for } d_{c,peak} \le d_n < -\frac{f_c}{K_{c,e}} \\ \frac{d_n - d_{c,u}}{d_{c,peak}+d_{c,u}}f_c & \text{for } d_{c,u} \le d_n < -d_{c,peak} \\ 0 & \text{for } d_n < d_{c,u} \end{cases} \tag{1}$$

where the constants B_1, B_2 and A can be calculated by:

$$B_1 = \left(\frac{A-2}{A} + 2\frac{A-1}{A}\frac{f_c}{K_{c,e}d_{c,peak} - f_c}\right)f_c \tag{2}$$

$$B_2 = \left(\frac{3-2A}{A} - 2\frac{A-1}{A}\frac{f_c}{K_{c,e}d_{c,peak} - f_c}\right)f_c \tag{3}$$

$$A = \left(\frac{K_{c,e}d_{c,peak}}{f_c}\right)^{\frac{1}{3}} \tag{4}$$

The ultimate relative displacement in compression $d_{c,u}$ depends on the compressive fracture energy $G_{f,c}$ and is given by Equation (5).

$$d_{c,u} = -d_{c,peak} - \max\left[0, \frac{2G_{f,c}}{f_c} - \frac{f_c}{A^2K_{c,e}} - \frac{A+1}{A}\left(d_{c,peak} - \frac{f_c}{K_{c,e}}\right)\right] \tag{5}$$

The unloading/reloading path is represented through a bilinear curve: when unloading from a stress state $\sigma_{c,limit}$, a linear branch with elastic stiffness $K_{c,e}$ is followed until a stress level $\sigma_\lambda = (1-\lambda)\sigma_{c,limit}$ is reached; then, a secant stiffness $K_{c,e,1}$ to the origin is used. The reloading follows the same path as the unloading. The unloading factor λ is defined such that $\lambda = 1$ corresponds to fully linear elastic unloading, whereas $\lambda = 0$ corresponds to secant unloading. The compressive behaviour is depicted in Fig. 1a.

2.2. Tension

The uni-axial tensile behaviour is described by an elastic ascending branch followed by linear softening (Eq. (6)), with the ultimate tensile relative displacement $d_{tu} = 2G_{ft}/f_t$ based on the tensile fracture energy G_{ft}. For unloading and reloading, secant stiffness is applied (Fig. 1b).

$$\sigma = \begin{cases} K_{t,e}d_n & \text{if } 0 \le d < d_{t,peak} \\ f_t - \frac{f_t}{d_{t,u} - d_{t,peak}}(d_n - d_{ft}) & \text{if } d_{t,peak} \le d < d_{t,u} \\ 0 & \text{if } d_{t,u} \le d \end{cases} \tag{6}$$

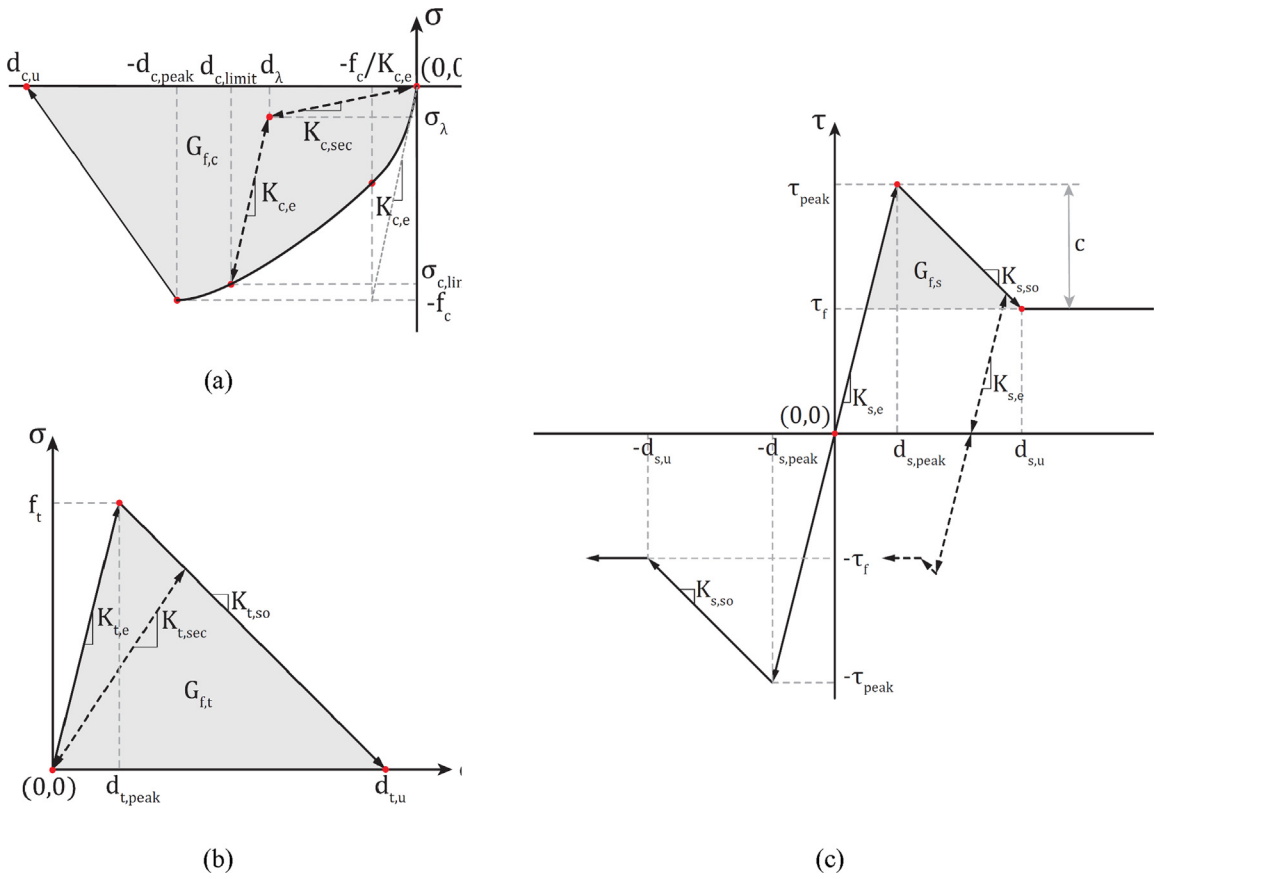

Fig. 1. Uniaxial constitutive curves for (a) compression, (b) tension and (c) shear for zero-thickness interface elements.

2.3. Shear

Finally, the shear behaviour is described by a trilinear envelope. Elastic behaviour is adopted until the shear capacity τ_{peak} is reached, followed by linear softening with stiffness $K_{s,so}$ until all the shear fracture energy G_{fs} is consumed and a residual shear strength ($\tau_f = \max(-\mu\sigma, 0)$) is reached. The shear strength is determined from Coulomb friction as: $\tau_{peak} = \max(c - \mu\sigma, c)$ where σ_n, c and μ are the normal stress, the cohesion and the friction coefficient, respectively. The shear unloading and reloading always follow the initial shear stiffness $K_{s,e}$, as shown by the dashed lines in Fig. 1c. The dilatancy angle is not taken into account in the definition of the constitutive law. This implies that a zero dilatancy angle is assumed, which is in accordance with the observation that the dilatancy angle tends to zero under increasing relative-shear-displacement and normal confining pressure ([1,41]). Moreover, in [8] it was shown that non-zero values of dilatancy angle may lead to over-stiff behavior and stress locking. For more information refer to [16,40].

$$\tau = \begin{cases} d_s K_{s,e} & \text{if } 0 \le |d_s| \le d_{s,peak} \\ \frac{d_s}{|d_s|}\tau_{peak} + (d_s - d_{s,peak})K_{s,so} & \text{if } d_{s,peak} < |d_s| \le d_{s,u} \\ \frac{d_s}{|d_s|}\tau_f & \text{if } d_{s,u} < |d_s| \end{cases} \quad (7)$$

where $d_{s,peak} = \frac{\tau_{peak}}{K_{s,e}}$ and $d_{s,u} = d_{s,peak} + \frac{2G_{fs}}{c} - \frac{c}{K_{s,e}}$.

For the biaxial state of combined shear and tension, both the tensile and shear capacity are lower than the corresponding uniaxial capacities, as explained in detail in Section 3.

3. Multi-surface damage-plasticity

The coupling effect between the normal and the shear stress of this constitutive model is defined by a multi-surface plasticity criterion, which includes a tension cut-off, a compression cut-off, and a Coulomb friction failure surface (Fig. 2).

The surfaces of Fig. 2 can also be expressed with three yield functions, as presented below.

$$\begin{cases} f_1 = |\tau| + \sigma \times tan\phi - c(1-w) \\ f_2 = \sigma - (1-w)f_t \\ f_3 = -(1-w_c)f_c - \sigma \end{cases} \quad (8)$$

where

w: the damage factor for cracking caused by tension and/or shear, with values varying between 0 and 1. The initial value is

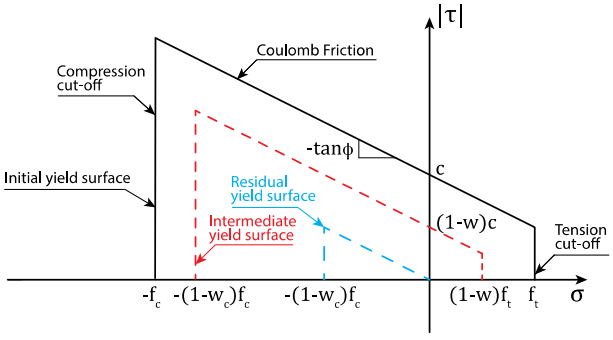

Fig. 2. Multi-surface plasticity criterion for interface elements.

equal to 0 and corresponds to an uncracked state, while the maximum value of 1 corresponds to fully damaged material;

w_c: the damage factor of crushing caused by compression, with values varying between 0 and 1. The initial value of w_c is 0 and remains 0 during pre-peak hardening, whereas it increases up to 1 during post-peak softening.

By definition, all stress states (combinations of σ and τ) should be within or on the yield surfaces, such that the values of functions f_1, f_2 and f_3 satisfy simultaneously the following criteria:

$$f_1 \leq 0, \quad f_2 \leq 0, \quad f_3 \leq 0 \tag{9}$$

Stress states inside the contour only cause elastic deformations, whereas stresses on the yield surface contribute to the evolution of plastic deformations. The yield surface expands during compressive hardening, and shrinks during compressive/tensile/shear softening. The damage factor w is used to couple the softening in tension and shear, resulting in a two-way dependency between the shear and tensile stresses. Similarly, the damage factor w_c relates to the softening rate in compression. Only one-way dependency exists between compression and shear: a change in the compressive capacity affects the shear capacity, whereas a change in the shear capacity does not influence the compressive capacity.

4. Sub-stepping damage-plasticity calculation

This paper introduces a sub-step based iterative constitutive model. In the case that damage occurs (or increases) in an integration point, the corresponding incremental relative displacements are divided in n sub-increments (n both in normal and shear direction). These sub-increments are applied in subsequent pairs (n pairs in total), until the total incremental relative displacement is reached for each direction (this procedure is named "sub-increment divider"). In each pair first the normal sub-increment is applied, followed by the shear one. The sequential application of sub-steps ensures the convergence of the calculated stress state to the solution, as if the increments of relative displacements in both normal and shear directions were applied simultaneously (Fig. 3).

Instead of conventional return-mapping algorithms, a sequential procedure that includes two algorithms, is used to calculate the stress state once damage develops. These algorithms, named "uniaxial damage calculation" and "extra damage iterative calulation", are applied in sequence for each sub-step. The former algorithm calculates the stresses (σ, τ) and the damage in the normal and shear directions (w, w_c), based on the uniaxial constitutive equations of Section 2. The latter is an iterative algorithm that computes the damage factor w by including the extra damage due to the two-way coupling between tension and shear and/or the one-way coupling between compression and shear. This damage is induced by the reduction of the maximum capacity in one direction (dir-1, either normal or shear) caused by the updated value of the stress in the other direction (dir-2). The procedure is iterated until convergence of the values of strength is reached both in dir-1 and dir-2.

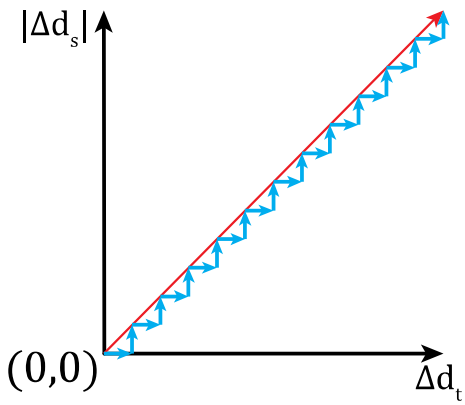

Fig. 3. Sequential application of sub-steps of the increments of relative displacements in shear and tensile direction.

As presented in Fig. 4, for each sub-step, first the damage in the normal direction is calculated. Then, the "extra damage iterative calulation" algorithm computes the additional damage caused in the shear and normal directions due to coupling. After convergence is achieved, the second part of the sub-step is applied, which includes the application of the shear displacement's sub-increment and the calculation of the corresponding damage. The iterative damage algorithm will then be used again to calculate the extra damage caused due to coupling first in the normal and then in the shear direction. In the next sub-step the same procedure is followed, until the total amount of normal and shear displacement has been applied. A detailed explanation of each of the two processes is provided in the following sections.

4.1. Uni-axial damage-plasticity loading

In the uniaxial damage calculation, the multi-surface plasticity criterion is first used to determine the maximum stress capacity in one direction (dir-1) based on the stress state of the other direction (dir-2). Then the stress and damage in dir-1 are calculated based on the following assumptions:

1. The softening stiffness ($K_{t,so}$ for tension and $K_{s,so}$ for shear) is kept constant and equal to the one introduced for uniaxial behaviour. However, due to coupling, the ultimate relative-displacement in one or both of the directions can change.
2. The amount of damage is calculated based on the increment of plastic relative-displacement (Eqs. (10) and (11)).

As already mentioned, the damage in tension and shear is coupled, meaning that the damage in one direction influences the capacity in the other direction. For a more straightforward demonstration of the uniaxial damage calculation algorithm in the case of tension and shear, one can refer to Fig. 5, where it is depicted how to further plastically load the interface's integration point in tension and shear, starting from four stress states A to D located already on the yield surface (Fig. 5a).

In Fig. 5:

$d_{i,0}$: the total relative normal or shear displacement of the last update;

$d_{i,1}$: the total relative normal or shear displacement of the current update;

σ_0 and τ_0: the total normal (tensile) and shear stress of the last update, respectively;

σ_1 and τ_1: the total normal (tensile) stress and shear of the current update, respectively;

$K_{i,e,0}$: the (softened) elastic tensile or shear stiffness of the last update;

$K_{i,so}$: the softening stiffness in tension or shear;

$d_{i,lost}$: the increment of plastic relative displacement in tension or shear. $d_{i,lost} = d_{i,1} - d_{i,0} \geq 0$, with $i = t$ for tension and $i = s$ for shear. The current damage factor w_1, common to tension and shear, is determined by Eqs. (10) and (11).

$$w_1 = min\left(w_0 + \frac{d_{t,lost}}{\frac{f_t}{K_{t,so}}}, 1\right) \tag{10}$$

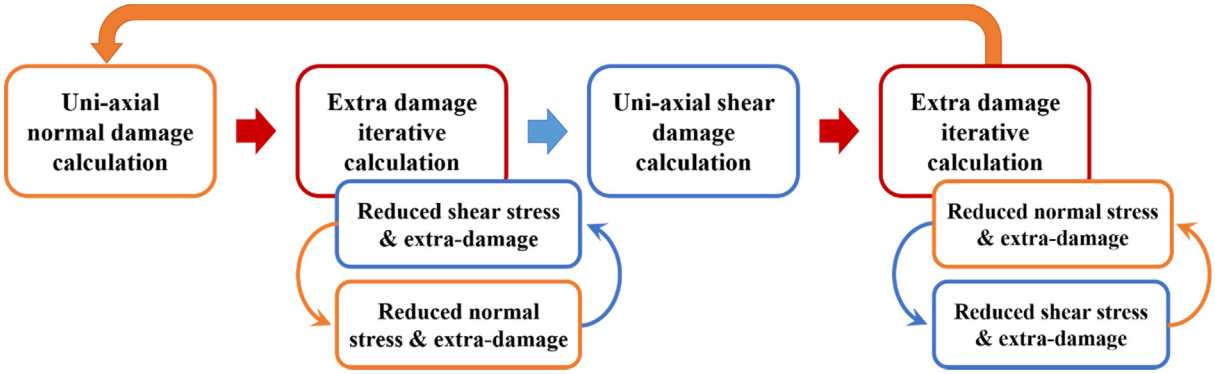

Fig. 4. Overview of the algorithm of the damage-plasticity calculation.

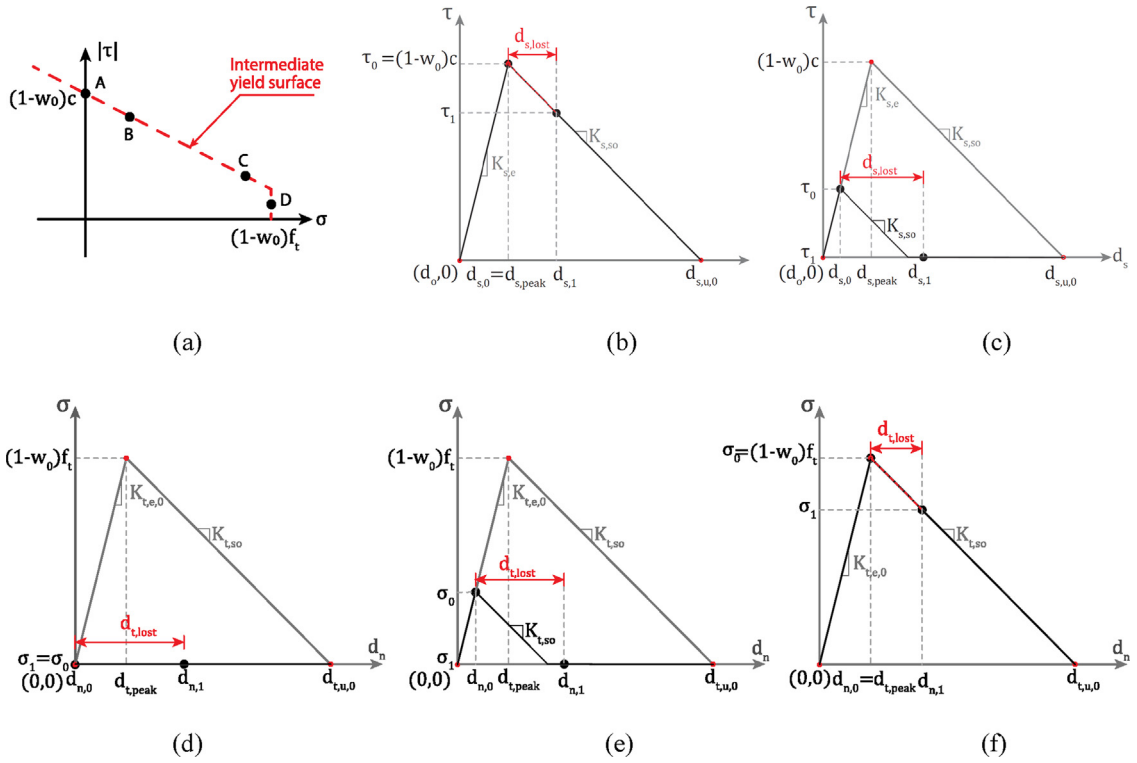

Fig. 5. Examples of uniaxial damage calculations: (a) possible initial stress states; (b) stress state A loaded in shear; (c) stress state C loaded in shear, (d) stress state A loaded in tension, (e) stress state B loaded in tension and (f) stress state D loaded in tension.

$$w_1 = min\left(w_0 + \frac{d_{s,lost}}{\frac{c}{K_{s,so}}}, 1\right) \tag{11}$$

In the case of compression, only the shear capacity is influenced by the level of compression: it increases during hardening and decreases during softening and unloading; this is discussed in Section 4.2. On the other hand, the compressive stress/strength/damage is not influenced by shear and the calculation of compressive damage factor is simple and given by

$$w_{c,1} = min\left(\frac{-f_c - \sigma_1}{-f_c}, 1\right) \tag{12}$$

where σ_1 is the compressive normal stress at the current step.

4.2. Extra damage iterative calculation

Softening in tension, and unloading or softening in compression lead to a reduction of the maximum shear capacity τ_{peak}, in which case the integration point might be unable to withstand the shear stress of the previous update (shear stress τ_0 at the beginning of the sub-step). Therefore, the value of the shear stress may further reduce (extra-softening) in order to reach a new equilibrium between the shear load and the shear capacity, or in other words, between the external shear force applied to the interface and the internal shear force of the interface. A similar situation can also occur for the tensile capacity after softening in shear; if the tensile capacity is not able to carry the tensile stress of the last update, extra damage in tension will occur before the next uniaxial damage is calculated in normal direction. The influence of one direction on the other (shear on normal -tension- and normal -tension or compression- on shear) is therefore computed through an iterative procedure, named extra-damage calculation, until convergence at the local integration point level is achieved.

A simple mechanical model is used to define the extra damage, consisting of two units stacked on top of each other, with a mortar layer in-between them, assuming that there is already a partially

developed crack along the mortar joint and that the block is further loaded in shear (or tension). The analytical derivation of the equations and their graphical representation can be found in APPENDIX A. The reduced shear stress τ_1 in the current sub-step after the additional softening (extra damage) can be expressed as:

$$\tau_1 = max\left(\tau_0 - \left(1 - \frac{K_{s,so}}{K_{s,e}}\right)(\tau_0 - \tau_{max}), \tau_f\right) \tag{13}$$

$$\tau_{max} = \max(-\sigma_0\mu + c(1 - w_0), 0) \tag{14}$$

Accordingly, the updated damage parameter after the additional softening is given as: $w_1 = w_0 + (\tau_{max} - \tau_1)/c$, where the indexes 0 and 1 represent the state before and after the extra-damage calculation, respectively.

Similarly, if the maximum tensile capacity σ_{max}, determined by the Coulomb friction criterion, is unable to resist the tensile stress σ_0 of the last update, the reduced tensile stress can be calculated as:

$$\sigma_1 = max\left(\sigma_0 - \left(1 - \frac{K_{t,so}}{K_{t,e}}\right)(\sigma_0 - \sigma_{max}), 0\right) \tag{15}$$

$$\sigma_{max} = min\left(\frac{c(1 - w_0) - \tau_0}{\mu}, f_t(1 - w_0)\right) \tag{16}$$

Therefore, the damage parameter w, that is the same for shear and tensile direction, can be updated as $w_1 = w_0 + (\sigma_{max} - \sigma_1)/f_t$.

4.3. Summary of constitutive model's procedure

The overall procedure of the proposed constitutive model is shown in Fig. 6. The algorithm of the sub-stepping damage-plasticity calculation, including the uni-axial plastic loading and iterative damage calculation algorithms, is implemented as the Sub-step divider and Plastic damage calculator in this model. The inputs of the user subroutine include the stresses and relative displacements in shear and normal directions of the previous step, the increments of the relative displacements of the current step, the loading/unloading/reloading status and all the material properties. The superscript 0 and 1 stand for the input and output values of the subroutine, respectively.

As for the sub-step divider, it is found that a minimum of two sub-steps are required. In order to optimize the sub-step iterative procedure and avoid unnecessary calculations the plastic damage calculator is initially calculated with two and three sub-steps and the damage factors for the two cases are compared. If the difference between the calculated results is within an established tolerance, these are the final results and the stiffness matrix is constructed. Otherwise, the number of sub-steps defined by the user is applied.

Finally, the stiffness matrix is calculated at the end of each iteration i, using the stresses and displacements calculated during the last sub-step. In particular, the tangent stiffness matrix is used, as described below:

$$K = \begin{bmatrix} \frac{\sigma_i - \sigma_{i-1}}{d_{n,i} - d_{n,i-1}} & 0 \\ 0 & \frac{\tau_i - \tau_{i-1}}{d_{s,i} - d_{s,i-1}} \end{bmatrix} \tag{17}$$

5. Validation

This constitutive model has been implemented in the finite element software DIANA FEA, version 10.3, via a user-supplied subroutine developed in FORTRAN. The validation of the constitutive model was carried out at structural level, by modelling five brick masonry walls. The first two walls modelled, were tested in TU Eindhoven, under monotonic in-plane conditions [42]: a Hollow Wall (a wall with a central opening) and a Solid Wall, both comprising solid clay bricks of dimensions 204 × 98 × 50 mm^3 and mortar joints of 10 mm thickness. The remaining three walls were tested in-plane in a quasi-static cyclic manner at the Stevin laboratory of TU Delft, and they were made of calcium-silicate bricks of dimensions 210 × 71 × 102 mm^3 with a mortar joint thickness of 12 mm. The walls are characterized by different geometries (aspect ratios of 0.7, 1 and 2.5), different boundary conditions (double clamped at top and bottom with or without possibility of vertical displacement at top, clamped at bottom only) and/or different precompression level. The walls exhibited different types of in-plane failure: shear failure or flexural failure [42,43] (see Table 1).

The finite element discretisations of the walls were composed of quadrilateral 4-noded, plane stress elements representing the bricks, and line interface elements (2 + 2 nodes) representing the head- and bed-joints. Linear elastic behavior was adopted for the bricks, except for the bricks of Solid Wall, where nonlinearities in tension and compression were introduced through a Total Strain Rotating Crack Model (TSRCM) (Table 2). The plane stress elements were integrated by a 2x2 Gauss scheme and the interface elements by a 2-point Newton-Cotes scheme. In the numerical model, the dimensions of the bricks were increased by the thickness of the adjacent mortar layer, in order to ensure geometrical compatibility with the zero-thickness interface elements, following a simplified micro-modelling approach.

The material properties used for walls TUD- COMP-3, COMP-4, and COMP-6 adopted the values measured during the experimental companion tests. These tests were performed both perpendicular and parallel to the bed joints, to investigate the orthotropic behavior and properties of masonry along its two predefined directions [37]. Accordingly, different material properties were used for the head and bed joints. (Tables 2 and 3).

As for the Solid and the Hollow Walls, the elastic and inelastic properties used by Lourenco et al. [1] were used, with the exception of the compressive strength and fracture energy of the interface elements. In Lourenco's model, a cap described by $f_3 = \sigma_2 + 9\tau^2 - \bar{\sigma}(\kappa_3)$ ensured the reduction of shear stresses for high compressive stresses. In the presented model, which does not include such a cap, the compressive strength of the interface elements was limited from 10.4 MPa to 4 MPa. This value was calculated through the abovementioned formula by setting $f_3 = 0$ and assuming that $\tau = c - \mu\sigma$, and $\bar{\sigma}(\kappa_3) = 10MPa$. As for the normal displacement at peak strength $d_{c,peak}$, it was calculated as follows: $d_{c,peak} = \frac{f_c}{3K_{c,e}} + \kappa_{fc}$, with $\kappa_{fc} = 0.09$, taken from [1].

The nonlinear tensile and shear properties of the interface can be interpreted as direct properties for debonding and shearing at micro-level, whereas the nonlinear compression properties for the interface should be regarded as lumped indirect properties that aim to phenomenologically represent the overall compressive behavior of the masonry as-a-composite. The actual compressive behavior may involve mortar crushing, brick splitting in the plane, brick splitting out of the plane, spalling and other effects. This is lumped into a fictitious discrete crush line characterized by an overall compressive strength and compressive fracture energy, estimated from the companion tests. The residual stiffness factor $ratio_{K,r}$ is defined as a percentage from the initial elastic interface stiffness to maintain slight residual stiffness after ultimate relative displacement, in order to avoid ill-conditioned stiffness matrices.

The dead weight and pre-compression load were applied in the first five load steps and were kept constant during the application of the cyclic lateral load on the top edge of the walls. For walls TUD- COMP-3 and COMP-4, the top edge of the wall was allowed to move vertically and was kept straight and horizontal, whereas

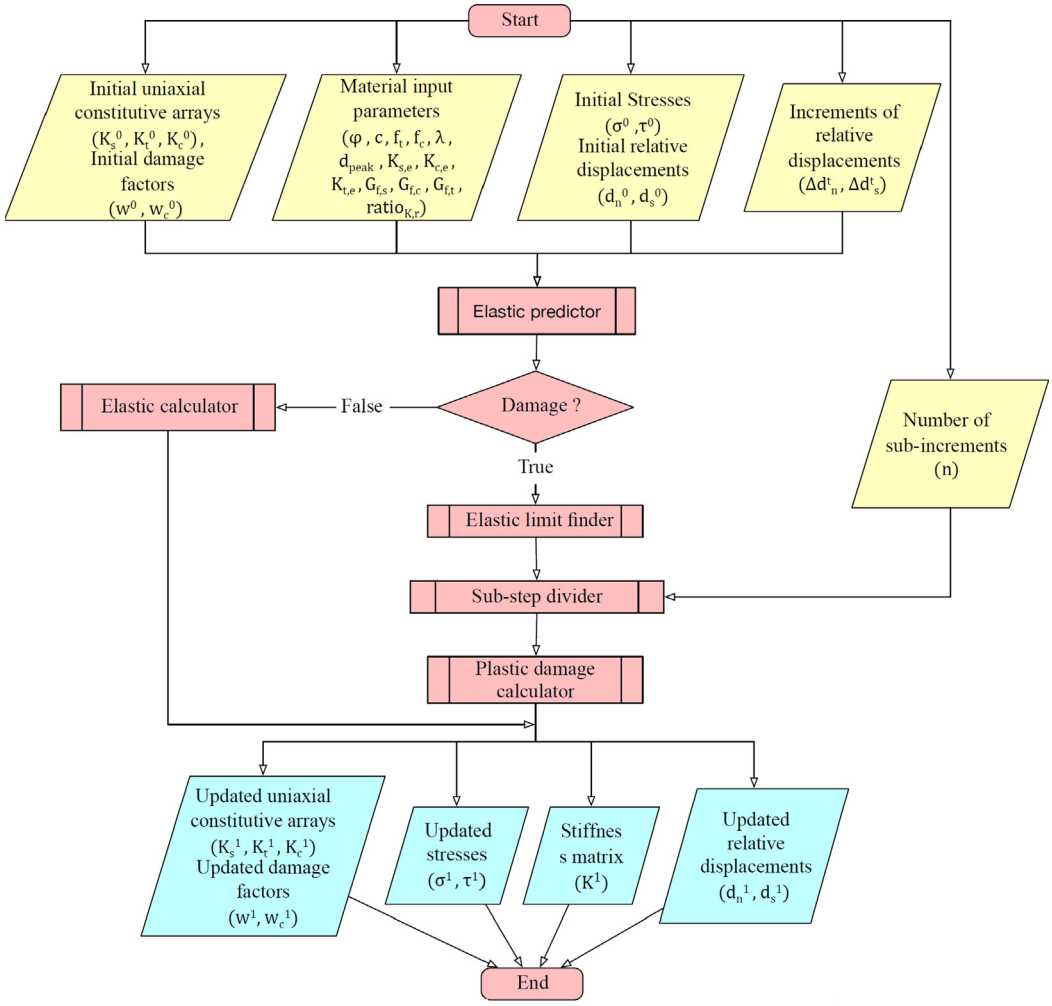

Fig. 6. Overview of the structure of the constitutive model.

Table 1
Geometrical properties, boundary conditions and main failure mechanism of the five modelled walls [42,43].

Name	Dimensions $L \cdot H \cdot t(mm^3)$	Aspect ratio (H/L)	Precompressionlevel(MPa)	Boundary conditions	Failure mode
Solid	$1000 \cdot 990 \cdot 98$	1.01	0.3	Double clamped	Shear
Hollow	$1000 \cdot 990 \cdot 98$	1.01	0.3	Double clamped	Shear and flexure
TUD-COMP-3	$1100 \cdot 2760 \cdot 102$	2.50	0.4	Double clamped ($\delta u_{y,top}$ allowed)	Flexure
TUD-COMP-4	$4000 \cdot 2760 \cdot 102$	0.7	0.3	Double clamped ($\delta u_{y,top}$ allowed)	Shear
TUD-COMP-6	$4000 \cdot 2760 \cdot 102$	0.7	0.5	Cantilever	Shear

Table 2
Input parameters for plane stress brick elements. The values in bold refer only to the solid wall; elastic behavior is assumed for the brick elements of the hollow wall.

Parameter modulus	Unit	TUD-COMP-3 & 4 & 6	Hollow & Solid Wall
Modulus of ElasticityE_{brick}	(MPa)	8990	16700
Poisson's ratioν	$(-)$	0.14	0.15
Densityρ	(T/mm^3)	1.805×10^{-9}	1.805×10^{-9}
Tensile strength$f_{t,brick}$	(MPa)	–	$-/2$
Fracture energy$G_{ft,brick}$	(N/mm)	–	$-/0.08$

for the Hollow and Solid Wals no vertical movement was allowed. Finally, for the cantilever wall TUD-COMP-6 the top edge was kept straight and was allowed to rotate.

Physically nonlinear, quasi-static analyses were performed with an implicit solver; a secant iteration scheme was chosen to ensure numerical stability at global level, with both displacement and force convergence norms to be satisfied and set to 0.01. The analyses would terminate when convergence was not reached, but all analyses were completed without convergence problems. Moreover, the number of user defined sub-steps, in the case that 2–3 sub-steps were not sufficient, was 100. Geometrical nonlinearities were neglected as they did not influence the results. The comparison with the experimental results was carried out in terms of total hysteretic behaviour and crack pattern at failure.

5.1. Hollow wall

Two identical double clamped walls with an opening (hollow walls) were tested in TU Eindhoven [42]. The opening resulted in

Table 3
Input material parameters for zero-thickness interface elements; the original material properties are used for the walls tested in TU Delft.

Parameter	Unit	TUD-COMP-3 & 4 & 6		Hollow & Solid	
		bed joint	head joint	bed joint	head joint
$K_{s,e}$	(MPa/mm)	39.31	16.36	36.00	36.00
$K_{t,e}$	(MPa/mm)	121.16	10.44	82.00	82.00
$K_{c,e}$	(MPa/mm)	121.16	10.44	82.00	82.00
$G_{f,s}$	(N/mm)	3.0	0.1	0.125	0.125
$G_{f,t}$	(N/mm)	0.00775	0.00078	0.018	0.018
$G_{f,c}$	(N/mm)	15.0	34.0	15	15
μ	$(-)$	0.43	0.43	0.75	0.75
c	(MPa)	0.140	0.014	0.35	0.35
f_t	(MPa)	0.1050	0.0035	0.25	0.25
f_c	(MPa)	5.93	8.10	4.0	4.0
$ratio_{K,r}$	$(-)$	10^{-4}	10^{-4}	10^{-4}	10^{-4}
λ	$(-)$	0.95	0.95	0.95	0.95
$d_{c,peak}$	(mm)	0.897	3.308	0.13	0.13

two small piers, and the tests resulted in different load–displacement curves, and different crack patterns. However, for both walls diagonal cracks initiated from the opening's corners and propagated towards the top and bottom of the wall in step-wise patterns. Subsequently, horizontal tensile cracks were also formed at the top and bottom of the piers. Eventually, failure due to toe-crushing occurred at the bottom and top of the wall [1,12]. The numerical model estimated with good accuracy the base shear capacity with respect to the one tested wall (-3.2%), whereas it overestimated it for the other wall by 23% (Fig. 9). Overall the softening behavior was in line with the experimental results. The numerical crack pattern resembled the experimental realistically, with diagonal cracks forming at top and bottom of the window and extending toward the corners of the wall. More specifically, the numerical crack pattern at the top half of the wall resembled the one of Panel J2G, whereas the bottom half of the wall resembled the one of Panel J3G (Figs. 7 and 8).

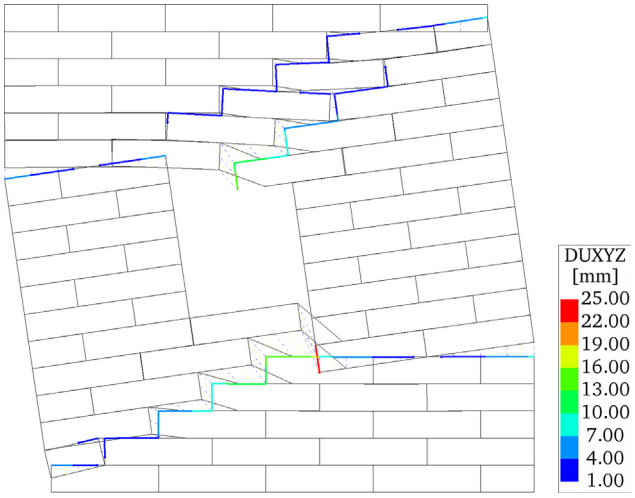

Fig. 8. Deformed shape and absolute values of relative displacements of the interface elements at the end of the numerical analysis for Hollow Wall (scaling factor 10).

5.2. Solid wall

The two tested solid walls formed initially horizontal cracks at the top and bottom of the wall. As the applied deformation increased, diagonal shear cracks prevailed, alongside with cracking of some bricks and toe crushing at the top and bottom corners (Fig. 10). Previous researchers modelled the potential cracks through the bricks with interface elements with satisfactory results. In this paper, instead, TSRCM is used for the modelling of the brick elements, with a tensile strength of 2 MPa and a fracture

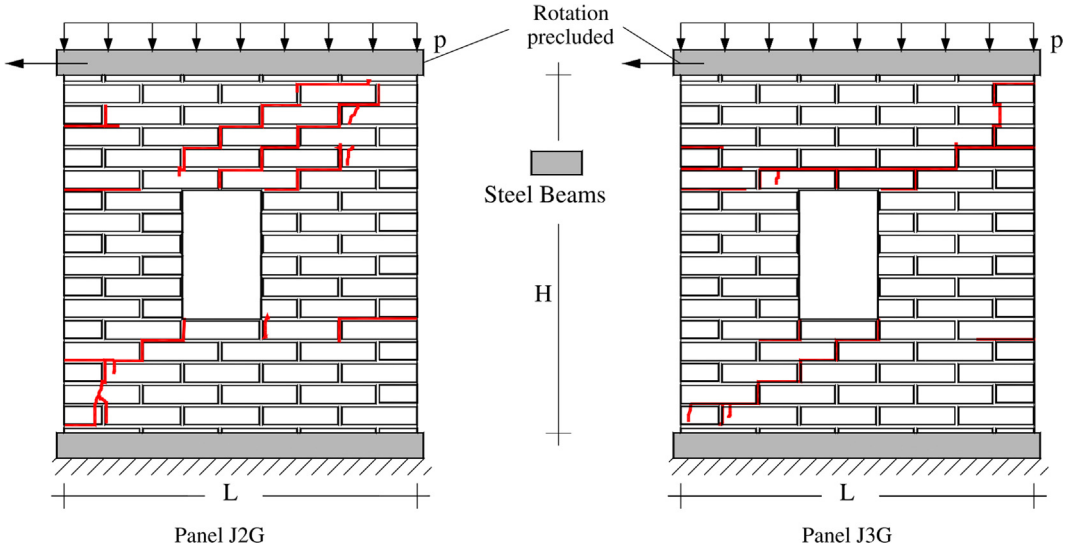

Fig. 7. Geometry and crack locations of the hollow walls observed at the end of the experiment, taken from [2].

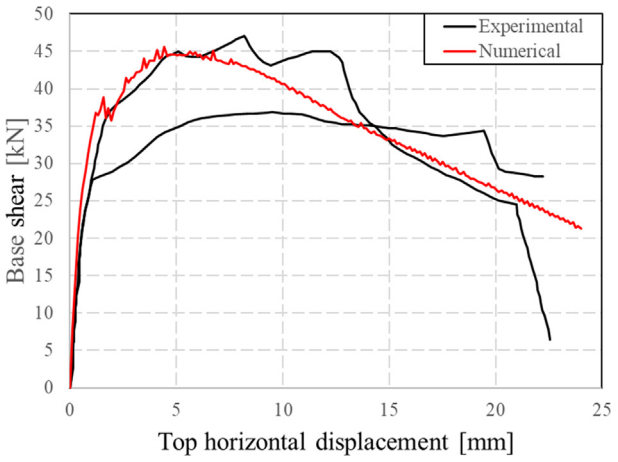

Fig. 9. Comparison of the experimental (black) and numerical (red) force–displacement capacity for Hollow Wall.

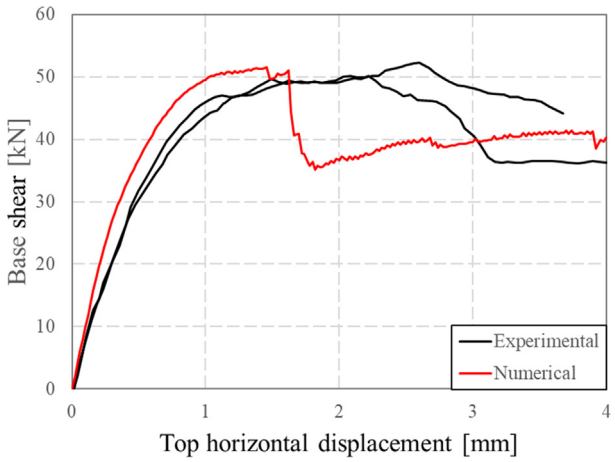

Fig. 12. Comparison of experimental (black) and numerical (red) results of solid wall.

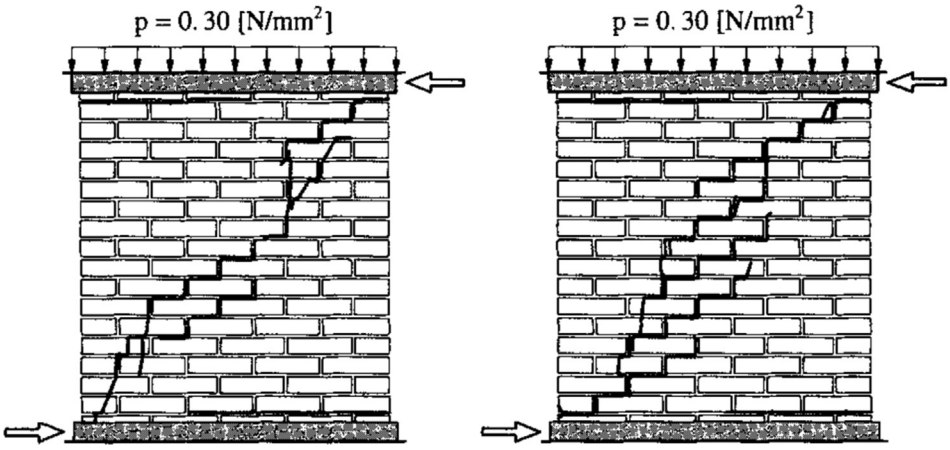

Fig. 10. Geometry and crack patterns of the solid walls as observed at the end of the experiments, taken from [1].

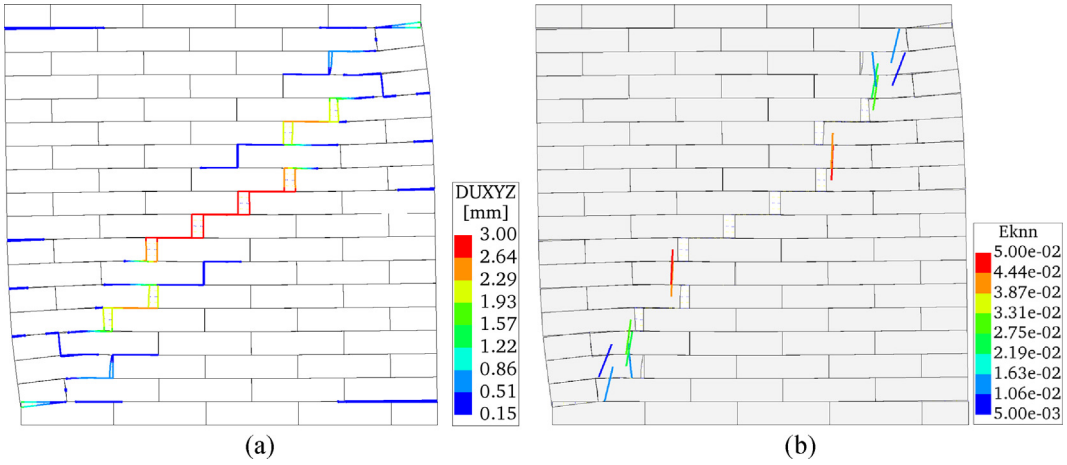

Fig. 11. Deformed shape of solid wall at the end of the numerical analysis, (a) displacement of interface elements, exhibiting the crack locations, and (b) location of cracks in brick elements and the corresponding cracking strains (scaling factor 10).

energy of 0.08 N/mm; the compressive behavior is assumed to be linear elastic. These values were used for the interface elements used to model the cracks in the bricks by [1], and were adopted here for plane-stress elements. The base shear capacity was predicted with very good accuracy, differing only by −1.4% and 2.7% from the experimental results. Moreover, the numerical residual strength fell between the two corresponding experimental values (Fig. 12). The sudden drop of the Force-Displacement curve occurred during the cracking of the first two bricks (depicted with red tensors in Fig. 11b)), and it occurred sooner than the more gradual drop observed for the experiments. Finally, in the numerical model, horizontal tensile cracks were formed at the top and bottom of the wall (similar to the experiment), followed by three diagonal step-wise cracks that formed at the centre of the wall and eventually expanded towards the corners. Cracking occurred in some brick elements as well (Fig. 11b).

5.3. TUD-COMP-4

TUD-COMP-4 was a double-clamped squat wall that exhibited pure shear failure. Its FE model captured well the failure mechanism, as well as the force capacity (+5.7%), the initial stiffness (+6.3%), the stiffness at the end of the loading procedure (+4.8%), and the energy dissipated throughout the test (+2.2%) (Fig. 14). In terms of crack pattern, the results from the experiment and the FE analysis were similar, with the diagonal cracks running from

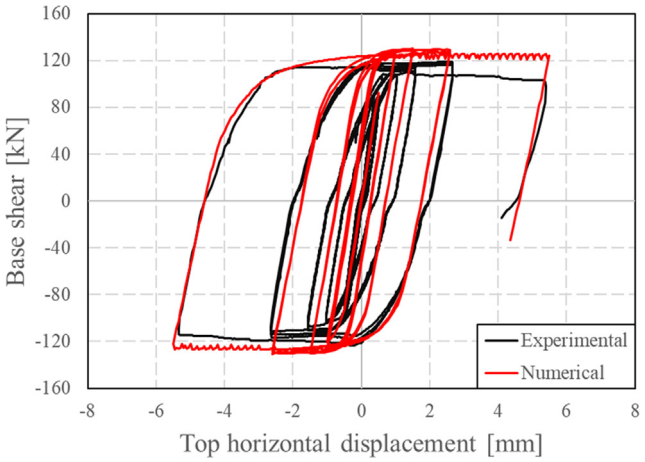

Fig. 14. Comparison of experimental (black) and numerical (red) force displacement diagram of wall TUD-COMP-4.

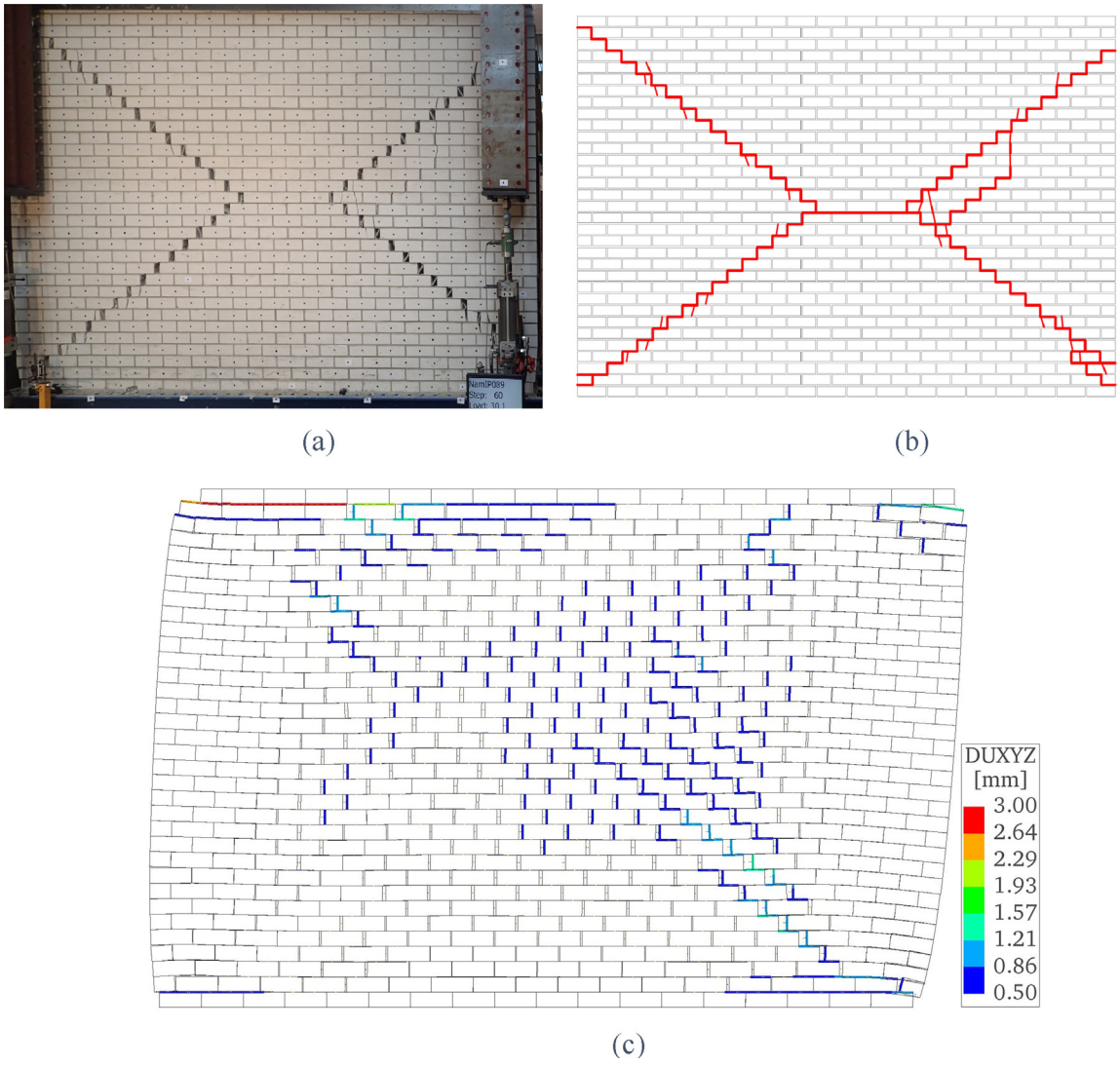

Fig. 13. (a) Wall TUD-COMP-4 at the end of the test, (b) crack pattern observed at the end of test TUD-COMP-4, and (c) deformed shape and absolute values of the relative displacements of the interfaces of TUD-COMP-4 for the maximum top displacement of 5.5 mm (scaling factor = 40).

the top to the bottom corners clearly visible (Fig. 13), although the experiment showed more localised cracks. This could have been due to the imperfections in the real wall, not taken into account in the numerical model. Besides, most of the micro-cracks in the real wall could not be observed with the naked eye. In terms of cyclic behaviour and dissipated energy, Fig. 14 shows that the analysis well reproduced the experiment. The unloading/reloading assumptions for shear, compression and tension, were concluded to adequately reproduce the cyclic behavior. Furthermore, as for all examples in this paper, the iterative damage calculation procedure performed adequately and in the global level the convergence criteria were met for all steps.

5.4. TUD-COMP-3

TUD-COMP-3 was a double-clamped slender wall, which exhibited flexural failure. The outcomes of the numerical analysis showed a good agreement in terms of initial stiffness with the

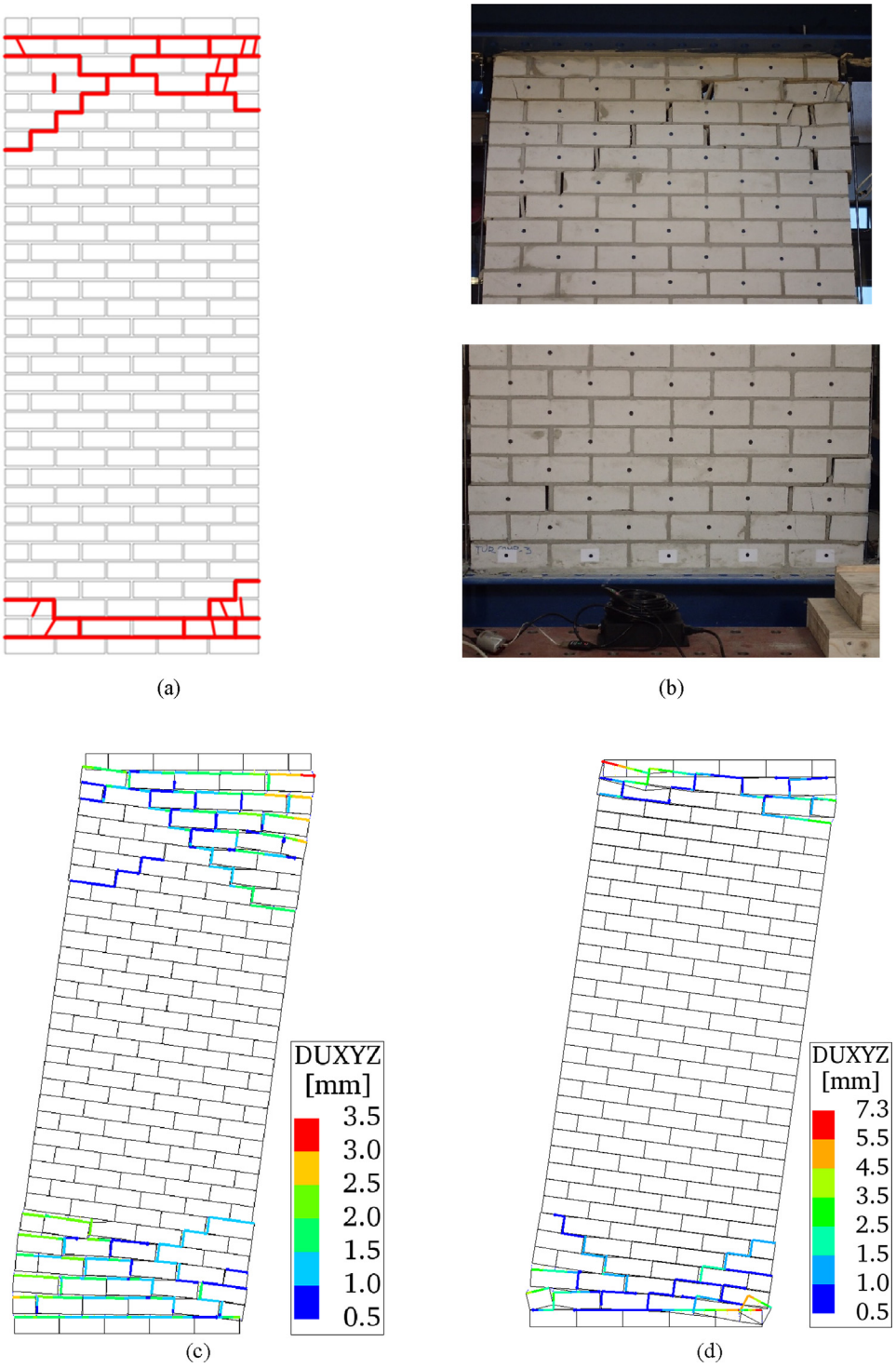

Fig. 15. (a) Observed crack pattern in the experiment of test TUD-COMP-3, (b) detail of cracking and crushing at top and bottom of the wall and absolute value of relative displacement of the interface at maximum lateral displacement for (c) uncalibrated and (d) calibrated TUD-COMP-3 ((scaling factor = 10).

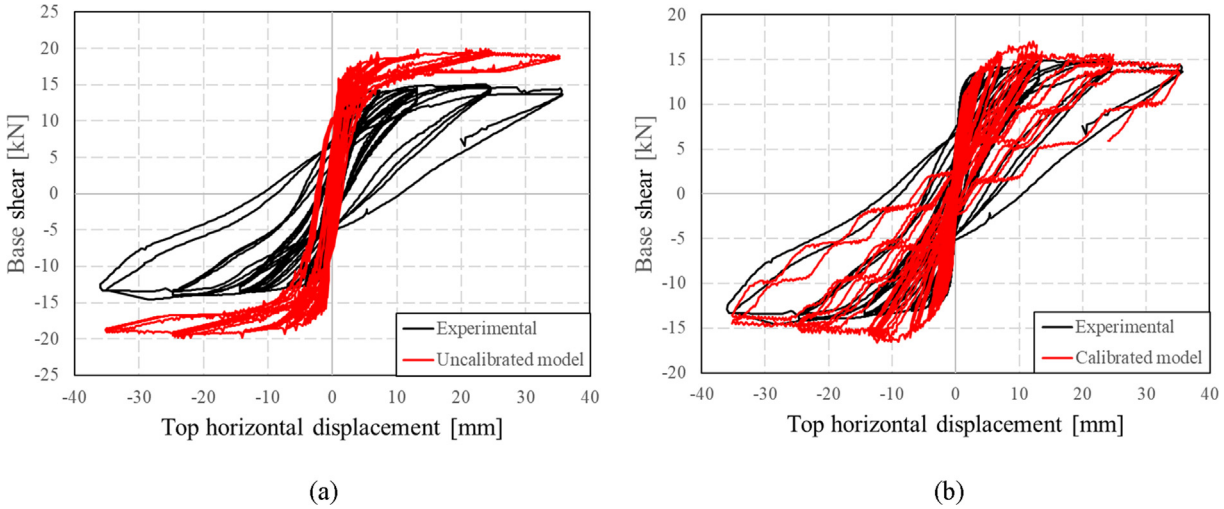

Fig. 16. Comparison of experimental (black) and numerical (red) force displacement diagram for the (a) uncalibrated and (b) calibrated DIANA simulation of wall TUD-COMP-3.

experimental result. However, the ultimate loading capacity was 25% higher than the experimental, and both the energy dissipation and the unloading stiffness were underestimated (Fig. 16a). The FE model showed a typical rocking behaviour with little toe crushing (Fig. 15c) while the experiment indicated a flexural behaviour with splitting of bricks at corners (Fig. 15b). In the performed analysis, the plane stress elements representing the bricks were modelled with a linear elastic constitutive model. To compensate for this limitation, the compressive strength of the zero-thickness interfaces was reduced further, to a relatively low value ($2MPa$) while the fracture energy under the softening branch was not changed. As mentioned before, the fictitious discrete crush lines aim to capture the overall compressive characteristics of the masonry. The calibrated model showed more toe crushing at the corner (Fig. 15d), accompanied by a reduction in the force capacity and a better agreement with the experiment in terms of loading capacity (+19.1%), initial stiffness (+0.8%), unloading stiffness at the end of the test (-4.7%), energy dissipation (-21.7%), and correct strength and stiffness degradation for repeated cycles of the same amplitude. It should also be noted that the reduced compressive strength, in combination with the choice of the unloading factor ($\lambda = 0.95$) caused accumulation of compressive deformation and damage in several integration points close to the top and the base of the wall. Moreover, the choice of the unloading/reloading factor as $\lambda = 0.95$ led to an initial rapid decrease of the compressive stress (and consequently shear stress) of these integration points upon unloading with elastic stiffness, followed by a sudden change in stiffness once the kink in the unloading curve is passed and secant stiffness towards the origin is adopted. This sudden change in the unloading stiffness may have caused the unusual stepped behavior that can be observed during the last cycles of the analysis, as shown in Fig. 16b.

5.5. TUD-COMP-6

Also the numerical simulation of TUD-COMP-6 (a cantilever, squat wall characterized by a combination of flexural and shear failure) was sensitive to the values adopted for the compressive strength. A first uncalibrated model, which used the original material properties of the wall, showed diagonal cracks that extended from the top corners and intersected at the bottom centre of the wall, extending all the way to the bottom edge. A long sliding plane developed at the right bottom edge with little crushing (Fig. 17c), whereas in the experiment toe crushing (in the form of mainly brick splitting) was more significant (Fig. 17a-b). This difference also resulted in a force–displacement curve that corresponded more to the typical pure sliding behaviour, deviating from the experiment. In a second, calibrated model, the compressive strength f_c was then reduced from 5.98 MPa to 4.5 MPa (fracture energy under the softening branch remains the same) and the friction coefficient μ was increased from 0.43 to 0.50. The calibrated model exhibited significantly more toe crushing at both bottom corners (Fig. 17d), even though the overall crack pattern still deviated from the experimental result. The force displacement curve showed a good agreement in terms of initial stiffness (-9.0%), ultimate capacity (+10.0) and energy dissipation (+7.0%), with some differences in the unloading stiffness at the end of the analysis. This reflects that the crushing of the corner interface elements can equivalently model the splitting of the bricks in the experiment. Again, global convergence was satisfied throughout the process.

6. Conclusions

In this paper a constitutive model for the in-plane behaviour of masonry line interface elements is proposed. The model combines elements of multi-surface plasticity and damage mechanics, using a sub-stepping algorithm to compute local damage and provide numerical stability, as an alternative to plasticity based return-mapping algorithms. The iterative sub-stepping algorithm is introduced to keep the calculated stress state on the yield surfaces while those are shrinking at the same time due to softening. To the author's knowledge, this technique has not been used before for masonry structures. Failure in shear, tension and compression are considered through a multi-surface damage-plasticity model, with a Coulomb friction criterion for shear, and tension and compression cut-off. Two independent damage parameters are included, one for compression and one for the coupling of tension and shear. The sub-stepping iterative algorithm ensures that during the damage calculation the fully-coupled tension-shear damage parameter is calculated consistently, with the updated stress state always lying on the yield surface defined by the damage parameters.

The comparison between experimental tests and the corresponding numerical simulations demonstrates that the developed model is capable of accurately simulating the behaviour of

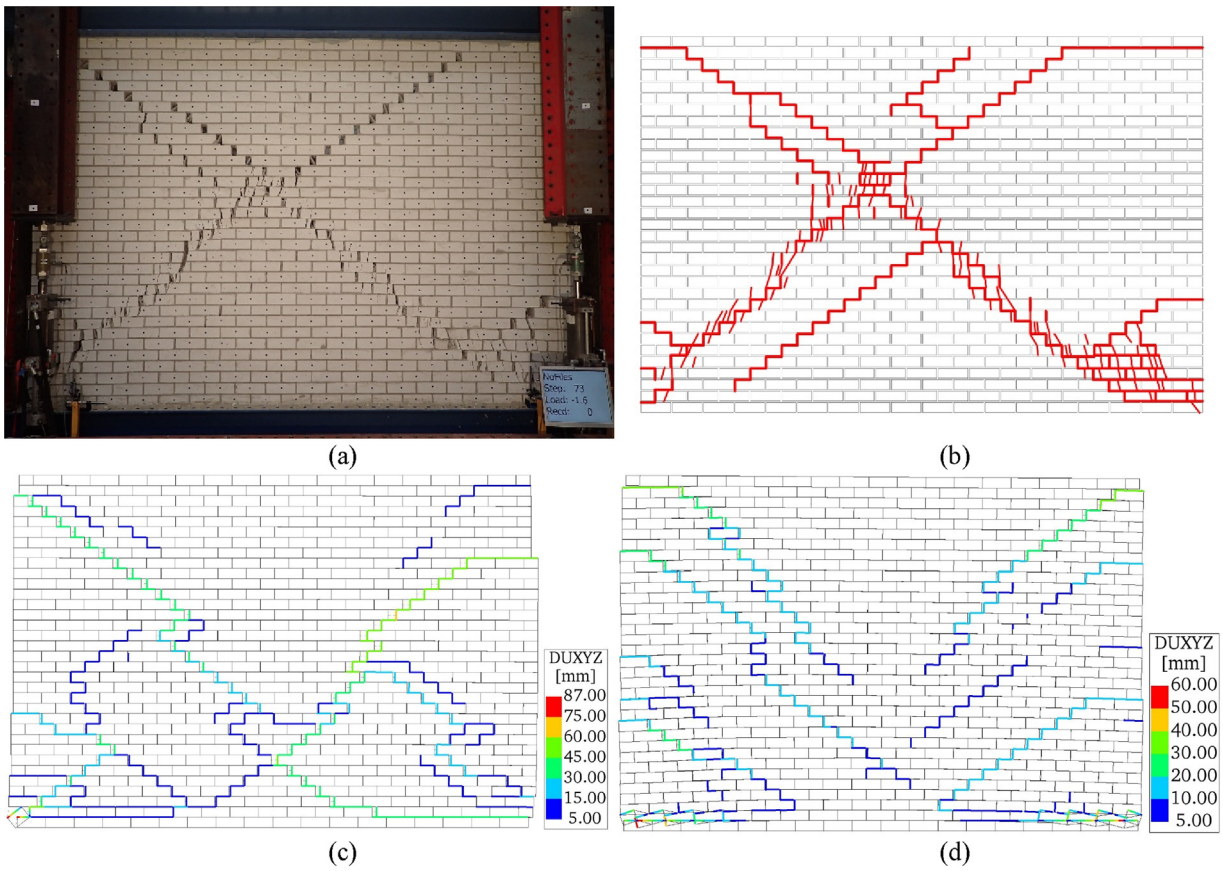

Fig. 17. (a) Observed crack pattern in the experiment of test TUD-COMP-6 and the absolute value of relative displacement of the interface at maximum lateral displacement for (b) uncalibrated and (c) calibrated TUD-COMP-6 (scaling factor = 1).

masonry walls subjected to lateral, in-plane loading in terms of failure mode, hysteretic behaviour and crack pattern. Moreover, the sub-stepping technique has been demonstrated to allow stable and robust analyses for all the tested cases.

From sensitivity studies, it was observed that the model is sensitive to the assumed value of the compressive strength of the mortar joint (Fig. 16 and Fig. 18), when toe-crushing is present. The use of the strength defined from companion tests performed at material level may lead to an underestimation of the toe-crushing failure. This issue can be solved by calibrating the material properties in compression, as done here, or by refining the compressive cap, coupling the maximum capacity of compression and shear.

The constitutive model is currently proposed for 2D analysis with line interface elements that connect plane stress elements, and it is planned to be extended towards 3D analysis with planar interface elements. Overall, the model proposed in this paper is

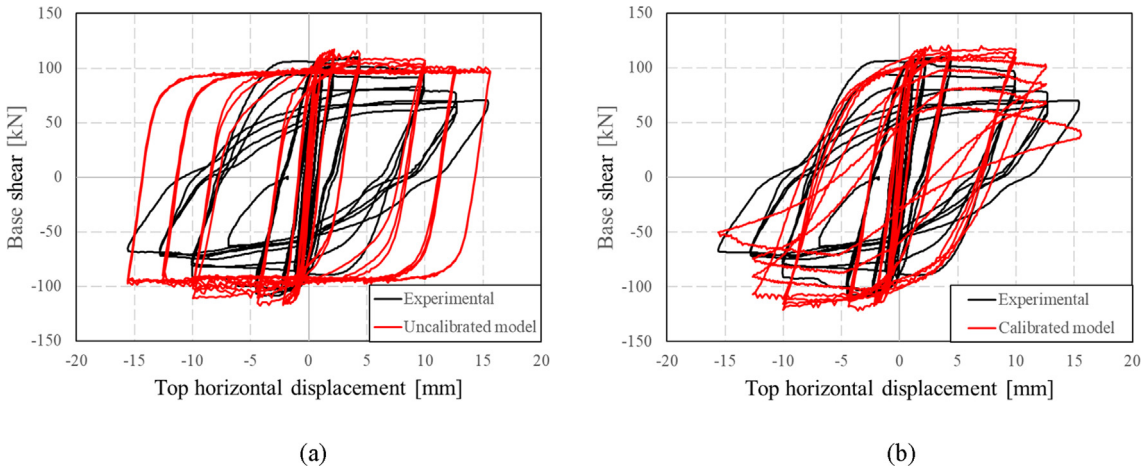

Fig. 18. Comparison of experimental (black) and numerical (red) force displacement diagram for the (a) uncalibrated and (b) calibrated DIANA simulation of wall TUD-COMP-6.

concluded to be an efficient and robust tool to analyse the in-plane cyclic behaviour of masonry walls, avoiding underestimation of hysteretic energy consumption observed in secant-based models and avoiding possible instabilities in return-mapping schemes for cornered yield criteria present in softening plasticity.

Declaration of Competing Interest

The authors declare that they have no known competing financial interests or personal relationships that could have appeared to influence the work reported in this paper.

Acknowledgements

The work presented in this paper was conducted as an independent research. There was a connection to the context provided by Nederlandse Aardolie Maatschappij (NAM) in project "Physical testing and modelling – Masonry structures Groningen" (contract number U146268) towards understanding the behaviour of masonry structures subjected to induced seismicity, which is gratefully acknowledged.

Appendix A

To derive the formulae used for the extra-damage calculator, a simple mechanical model composed of two units and a mortar joint is considered (Fig. A.1). It should be assumed that, in the previous step, the structure has been loaded until a crack was partially developed (the green solid line and the blue dashed line in Fig. A.1). The current shear stress of the FE model is τ_0.

The application of the relative displacement in the normal direction (first sub-increment) reduces the maximum shear capacity of the interface element, to the value τ_{max}. However, the internal shear stress of the interface element has also decreased, that is why the plane stress elements representing the units after loading in normal direction (red dashed line) rebound a little bit compared with their original shape (blue dashed line). For the interface, a new equilibrium forms between the internal force of the interface element and the external force applied by the plane stress element to the interface element.

During this rebound process, a certain amount of additional softening has taken place. To calculate a reasonable value of the shear stress after softening, the detailed mechanical model is considered. The deformed shape of the mechanical model after softening is plotted with orange solid lines in the scaled figure. The relative displacement of the crack increases from $d'_{s,0}$ to $d'_{s,1}$ (detail of Fig. A.1). Given that the relative shear displacement of the interface element does not change and the units in the mechanical model are always overlapped with the corresponding part of the units in the FE model throughout the entire loading process, the value of $d'_{s,1}$ can be calculated using the geometrical compatibility equation as follow:

$$d'_{s,1} = d'_{s,0} + \frac{\tau_0}{G_j}h_j - \frac{\tau_0}{G_u}h_j + \frac{\tau_{1,e}}{G_u}h_j - \frac{\tau_{1,e}}{G_j}h_j \tag{A.1}$$

where

$d'_{s,1}$: the relative displacement of the cracked surface in shear direction in the mechanical model after the additional softening;

$d'_{s,0}$: the relative displacement of the cracked surface in shear direction in the mechanical model before the additional softening;

$\tau_{1,e}$: the elastic shear stress in the intact mortar layer during the rebound process of the additional softening;

τ_0: the shear stress before the additional softening;

G_u: the shear modulus of the unit in the mechanical model;

G_j: the shear modulus of the mortar joint in the mechanical model;

h_j: the total height of the mortar joint in the mechanical model.

It should be noted that the shear stresses are the same for both the mechanical model and the FE model. Also, from the geometrical compatibility condition of the mechanical model in the elastic stage, the following equation can be derived:

$$\frac{1}{K_{s,e}} = \frac{h_j}{G_j} - \frac{h_j}{G_u} \tag{A.2}$$

where $K_{s,e}$ is the elastic stiffness of the zero-thickness interface element in FE model in shear direction. Combined with the Eq. (A.2), Eq. (A.1) can be rewritten as

$$\Delta d'_s = d'_{s,1} - d'_{s,0} = h_j\left(\frac{1}{G_u} - \frac{1}{G_j}\right)(\tau_{1,e} - \tau_0) = -\frac{1}{K_{s,e}}(\tau_{1,e} - \tau_0) \tag{A.3}$$

where $\Delta d'$ is the increment of the relative displacement of the cracked surface in the mechanical model.

The above equation indicates the relation between the shear stress in the intact mortar layers and the increment of the relative

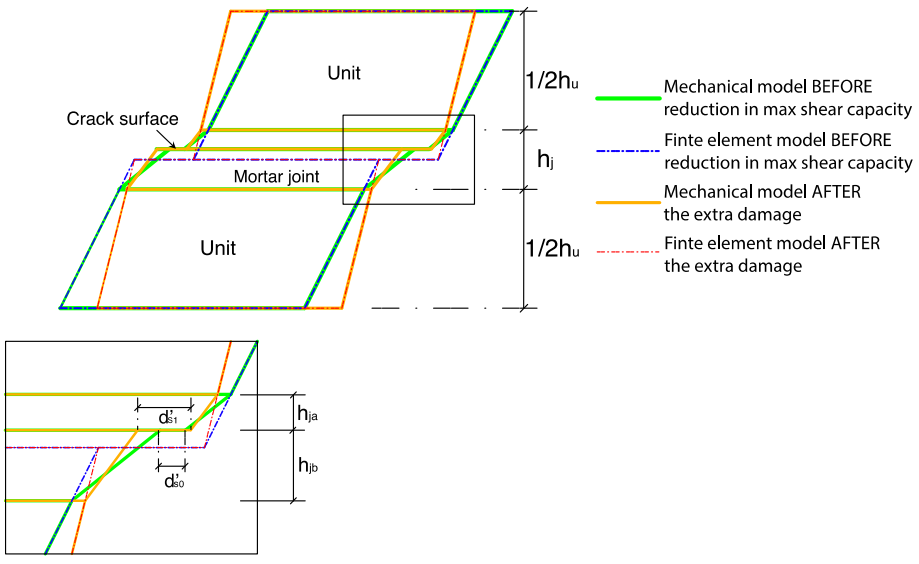

Fig. A1. Illustration of the extra damage process of the partially cracked mechanical model and FE model.

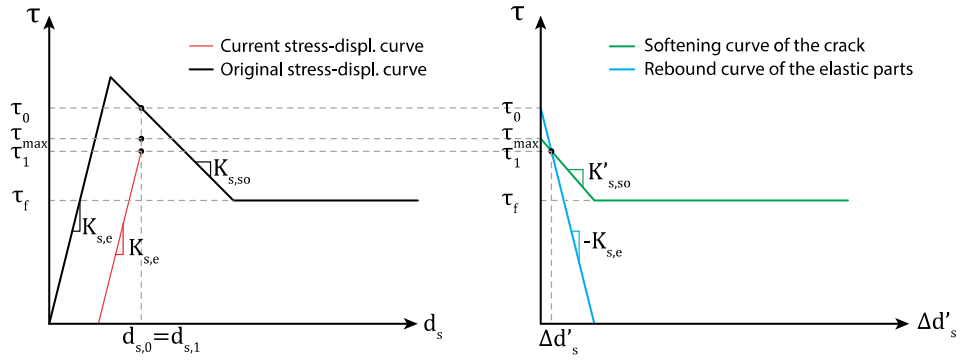

Fig. A2. Relation between the amount of softening at the interface element and the relative displacement of the real crack in shear.

displacement of the cracked surface during the rebound process. The internal shear stress in the intact mortar layers is also equal to the external shear stress applied on the cracked surface.

In addition, the following equation relates the internal shear stress of the cracked surface during its softening process to the increment of the relative displacement of that surface. That is:

$$\tau_{1,so} = max(\tau_{max} + K'_{s,so}\Delta d'_s, \tau_f) \tag{A.4}$$

where

$K'_{s,so}$: the softening stiffness of the cracked surface in the mechanical model in shear direction (negative). Its value can be calculated with $\frac{1}{K_{s,so}} = \frac{1}{K_{s,e}} + \frac{1}{K'_{s,so}}$;

$\tau_{1,so}$: the shear stress in the cracked surface during the additional softening;

w_0: damage factor of the crack caused by shear and tension before the additional softening, $0 \leq w_0 \leq 1$.

The Eqs.ations (A.3) and (A.4) are plotted in Fig. A.2 in blue and green color respectively.

Knowing that the internal stress $\tau_{1,so}$ and the external stresses $\tau_{1,e}$ of the cracked surface must be equal to each other ($\tau_{1s0} = \tau_{1,e} = \tau_1$), the reduced shear stress τ_1 in the current substep after the additional softening (extra damage) can therefore be calculated as the intersection of these two lines. This can be solved by combining these two Eqs. (A.3) and (A.4) resulting in Eq. (13).

References

[1] Lourenço PB, Rots JG. Multisurface interface model for analysis of masonry structures. J Eng Mech 1997;123(7):660–8.
[2] Milani G. Simple homogenization model for the non-linear analysis of in-plane loaded masonry walls. Comput Struct 2011;89(17):1586–601.
[3] Roca P et al. Structural Analysis of Masonry Historical Constructions. Classical and Advanced Approaches. Arch Comput Methods Eng 2010;17(3):299–325.
[4] Asteris PG, et al. Numerical Modeling of Historic Masonry Structures. In Handbook of Research on Seismic Assessment and Rehabilitation of Historic Structures; 2015, p. 213–56.
[5] D'Altri AM et al. Modeling Strategies for the Computational Analysis of Unreinforced Masonry Structures: Review and Classification. Arch Comput Methods Eng 2019.
[6] Lourenço PB. Computational strategies for masonry structures. Civil Engineering and Geosciences. Delft: Delft University of Technology; 1996.
[7] Lourenço PB. Computations on historic masonry structures. Prog Struct Mat Eng 2002;4(3):301–19.
[8] Rots JG et al. Structural masonry: an experimental/numerical basis for practical design rules. Rotterdam: Balkema; 1994.
[9] Berto L et al. An orthotropic damage model for masonry structures. Int J Numer Meth Eng 2002;55(2):127–57.
[10] Cervera M. A smeared-embedded mesh-corrected damage model for tensile cracking. Int J Numer Meth Eng 2008;76(12):1930–54.
[11] Lotfi H, Shing P. An appraisal of smeared crack models for masonry shear wall analysis. Comput Struct 1991;41(3):413–25.
[12] Lourenço PB, de Borst R, Rots JG. A plane stress softening plasticity model for orthotropic materials. Int J Numer Meth Eng 1997;40(21):4033–57.
[13] Papa E, Nappi A. Numerical modelling of masonry: A material model accounting for damage effects and plastic strains. Appl Math Model 1997;21(6):319–35.
[14] Pelà L et al. A localized mapped damage model for orthotropic materials. Eng Fract Mech 2014;124:196–216.
[15] Pelà L, Cervera M, Roca P. An orthotropic damage model for the analysis of masonry structures. Constr Build Mater 2013;41:957–67.
[16] Rots JG et al. Computational modelling of masonry with a view to Groningen induced seismicity. Struct Anal Hist Constr Anamn Diagn Ther Contr 2016:227–38.
[17] Saloustros S et al. An enhanced finite element macro-model for the realistic simulation of localized cracks in masonry structures: A large-scale application. Int J Archit Herit 2018;12(3):432–47.
[18] Lotfi HR, Shing PB. Interface model applied to fracture of masonry structures. J Struct Eng 1994;120(1):63–80.
[19] Oliveira DV, Lourenço PB. Implementation and validation of a constitutive model for the cyclic behaviour of interface elements. Comput Struct 2004;82(17–19):1451–61.
[20] Gambarotta L, Lagomarsino S. Damage Models for the Seismic Responce of brick masonry shear walls. Part 1: the mortar joint model and its applications. Earthquake Eng Struct Dyn 1997;26(4):423–39.
[21] Giambanco G, Rizzo S, Spallino R. Numerical analysis of masonry structures via interface models. Comput Meth Appl Mech Eng 2001;190(49–50):6493–511.
[22] van Zijl GPAG. Modeling Masonry Shear-Compression: Role of Dilatancy Highlighted. J Eng Mech 2004;130(11):1289–96.
[23] Alfano G, Sacco E. Combining interface damage and friction in a cohesive-zone model. Int J Numer Meth Eng 2006;68(5):542–82.
[24] Chaimoon K, Attard MM. Modeling of unreinforced masonry walls under shear and compression. Eng Struct 2007;29(9):2056–68.
[25] Lourenço PB. Recent Advances in Masonry Modelling: Micromodelling and Homogenisation. In Multiscale Modeling in Solid Mechanics; 2009, p. 251–94.
[26] Zhang S et al. Micro-mechanical finite element modeling of diagonal compression test for historical stone masonry structure. Int J Solids Struct 2017;112:122–32.
[27] D'Altri AM et al. A 3D detailed micro-model for the in-plane and out-of-plane numerical analysis of masonry panels. Comput Struct 2018;206:18–30.
[28] Minga E, Macorini L, Izzuddin BA. A 3D mesoscale damage-plasticity approach for masonry structures under cyclic loading. Meccanica 2018;53(7):1591–611.
[29] Pulatsu B et al. Discontinuum analysis of the fracture mechanism in masonry prisms and wallettes via discrete element method. Meccanica 2020;55(3):505–23.
[30] Huang J, Griffiths D. Observations on return mapping algorithms for piecewise linear yield criteria. Int J Geomech 2008;8(4):253–65.
[31] Adhikary DP et al. A robust return-map algorithm for general multisurface plasticity. Int J Numer Meth Eng 2017;109(2):218–34.
[32] Huang J, Griffiths D. Return mapping algorithms and stress predictors for failure analysis in geomechanics. J Eng Mech 2009;135(4):276–84.
[33] Lee J, Fenves GL. A return-mapping algorithm for plastic-damage models: 3-D and plane stress formulation. Int J Numer Meth Eng 2001;50(2):487–506.
[34] Sloan SW, Abbo AJ, Sheng D. Refined explicit integration of elastoplastic models with automatic error control. Eng Comput 2001.
[35] Wang W et al. A sub-stepping approach for elasto-plasticity with rotational hardening. Comput Mech 2006;37(3):266–78.
[36] Potts D, Ganendra D. An evaluation of substepping and implicit stress point algorithms. Comput Meth Appl Mech Eng 1994;119(3–4):341–54.
[37] Sloan SW. Substepping schemes for the numerical integration of elastoplastic stress–strain relations. Int J Numer Meth Eng 1987;24(5):893–911.
[38] Feenstra PH et al. A 3D constitutive model for concrete based on a co-rotational concept. Euro-C Conference Computational Modelling of Concrete Structures. Balkema; 1998.
[39] Feenstra PH, De Borst R. A plasticity model and algorithm for mode-I cracking in concrete. Int J Numer Meth Eng 1995;38(15):2509–29.
[40] Schreppers GMA, et al. DIANA validation report for masonry modelling. DIANA FEA BV & TU Delft: Delft; 2016.

[41] Pluijm vdR. Out-of-plane bending of masonry: behaviour and strength. Eindhoven: Technische Universiteit Eindhoven; 1999.
[42] Raijmakers TMJ, Vermeltfoort AT. Deformation controlled tests in masonry shear walls. Delft, The Netherlands: TNO-Bouw; 1992.
[43] Messali F et al. Experimental investigation of the in-plane cyclic behaviour of calcium silicate brick masonry walls. Bull Earthq Eng 2020:1–32.